Thermal conductivity and terahertz vibrational dynamics of vitreous silica

G. Baldi*
INFM-CNR CRS-SOFT Operative Group in Grenoble, c/o ESRF, Boîte Postale 220, F-38043 Grenoble Cedex, France

V. M. Giordano, G. Monaco, and F. Sette
European Synchrotron Radiation Facility, Boîte Postale 220, F-38043 Grenoble Cedex, France

E. Fabiani
Département des Technologies pour la Biologie et la Santé, CEA-Léti and Minatec, Grenoble Cedex 9, France

A. Fontana
Department of Physics, Trento University, Via Sommarive 14, 38050 Povo, Trento, Italy
and INFM-CNR CRS-SOFT, c/o Roma University "La Sapienza," 00185 Roma, Italy

G. Ruocco
Department of Physics and INFM-CNR CRS-SOFT, c/o Roma University "La Sapienza," 00185 Roma, Italy
(Received 19 February 2008; revised manuscript received 14 May 2008; published 27 June 2008)

The dynamic structure factor of vitreous silica is measured at terahertz frequencies by inelastic scattering of x rays (IXS) and neutrons (INS). The IXS experiment is performed at exchanged wave vectors q between 4 and 15 nm^{-1} and at temperatures above and below the glass transition. The neutron time-of-flight technique is used as a high-resolution probe in a comparable q region. The data analysis confirms the presence of two inelastic features in the IXS spectra in the entire explored wave-vector range. The lower-frequency component is nondispersive and is observed by both IXS and INS around the boson peak frequency. The higher-frequency one, associated with the longitudinal-acoustic-like branch, is marked by a positive dispersion, confirming the results of a previous study [Ruzicka *et al.*, Phys. Rev. B **69**, 100201 (2004)]. As q increases, the vibrational modes of the disordered structure progressively lose their plane-wave character; for q around that of the first sharp diffraction peak, the dynamic structure factor converges to an effective density of vibrational states. The contribution of the terahertz vibrations to the thermal conductivity of vitreous silica is then evaluated by means of a Kubo-type formula for the diffusivity in disordered systems. The acousticlike modes that persist at terahertz frequencies represent a heat conduction channel which accounts for only a fraction, although relevant, of the thermal conductivity. The failure of this approach to fully describe the conductivity data is attributed to the nondiagonal elements of the heat current operator that are not experimentally accessible.

DOI: 10.1103/PhysRevB.77.214309 PACS number(s): 63.50.−x, 65.60.+a, 61.05.cf, 61.05.fg

I. INTRODUCTION

Amorphous solids are defined by the lack of long-range structural order. The absence of translational invariance gives rise to a complex phenomenology in the vibrational properties of glasses and supercooled liquids. Macroscopically this complexity is reflected in anomalies in the thermal properties,[1] which distinguish the amorphous materials from the corresponding crystalline structures.

Vitreous silica is considered the prototype of strong glasses[2] and a model for the typical glass. Its vibrational dynamics has been widely investigated both experimentally[3–17] and by means of computer simulations.[18–23] Previous inelastic-neutron-scattering (INS) studies have focused on the determination of the density of vibrational states[7,10] and on the wave vector[8,11] q and on the frequency[12] dependence of the dynamic structure factor $S(q,\omega)$. The inelastic x-ray scattering (IXS) technique with meV energy resolution[13] has opened the possibility of measuring the Brillouin doublet at exchanged wave vectors on the order of a fraction of q_0, the position of the first sharp diffraction peak in the static structure factor.

The main results of the IXS experiments in v-SiO_2 can be summarized as follows:[14,24]

(i) Acousticlike excitations show up in the $S(q,\omega)$. At the lowest exchanged wave vector at present accessible to IXS, $q \sim 1$ nm^{-1}, the excitations propagate at the adiabatic longitudinal speed of sound.

(ii) At higher wave vectors, $q \geq 4$ nm^{-1}, a second peak, almost nondispersive, appears in the $S(q,\omega)$.

(iii) The appearance of the second excitation is associated with a positive dispersion of the sound velocity of the longitudinal-acoustic-like mode.

(iv) The damping of the longitudinal mode shows a quadratic dependence on q in the low wave-vector range, $q \leq 4$ nm^{-1}.

(v) The dispersion of the longitudinal mode reaches its maximum at wave vectors $q \sim q_0$. This behavior has been confirmed by classical molecular-dynamics (MD) simulations.[20,22]

The simultaneous presence of two peaks in the $S(q,\omega)$ has been observed in IXS experiments on other amorphous substances, such as water[25] and glassy glycerol.[26] The anomalous positive dispersion effect has been measured, on the contrary, only in vitreous silica,[14] although discrepancies

between the high- and low-frequency speeds of sound have been reported also for other materials, such as vitreous Se (Ref. 27) and a metallic glass.[28] A positive dispersion in the nonergodic glassy phase cannot be attributed to the structural (or α-) relaxation process, which takes place on a time scale many orders of magnitude longer than the one accessible to the x-ray probe.[29] Various computer simulation studies[19,20,30–32] have investigated the nature of this effect. In an MD simulation of a glassy Lennard-Jones system,[32] the positive dispersion was attributed to the onset of a microscopic (or μ-) relaxation process, defined in a harmonic description of the $S(q,\omega)$. The effect was thus explained as arising from the structural disorder of the amorphous network, suggesting its temperature independence.

The present work is devoted to a combined IXS-INS investigation of the terahertz dynamics in vitreous silica aiming to clarify this point. The IXS experiment is performed at temperatures above and below the glass transition temperature, $T_g = 1450$ K, in the exchanged wave-vector range between 4 and 15 nm^{-1} in order to verify whether the positive dispersion is indeed temperature independent. The INS time-of-flight spectroscopy is used as a high-resolution probe of the lower-frequency range in a comparable momentum window. A detailed line-shape analysis is performed in order to determine the main parameters describing the measured spectra. The present investigation confirms the harmonic nature of the high-frequency dynamics and indicates the structural disorder as responsible for both the broadening of the peaks and their shift with respect to a linear dispersion.

The existence of well defined acousticlike vibrations at terahertz frequencies naturally suggests their importance as heat conduction channels. Various attempts were done in the past to describe the thermal conductivity at high temperatures,[33–39] above the plateau region located around 10 K. The proposed models were affected by the lack of experimental information on the high-frequency vibrational dynamics. In this work we will present a comparison between the mean free path deduced from the IXS data and the high-temperature thermal conductivity. The analysis shows the relevance of the high-frequency modes as heat conduction channels, although they cannot account for the entire thermal conductivity. This discrepancy is attributed to a diffusion process among different eigenstates, as suggested by Allen and Feldman.[40]

The paper is organized as follows: In Sec. II the setup of the IXS and INS experiment is described. A brief introduction to the two techniques is followed by the presentation of the results. Section III is devoted to the description of the analysis of the experimental spectra. In Sec. IV the possible description of the dynamics in terms of dispersion curves and the evolution of the dynamic structure factor toward the density of vibrational states are discussed. The connection between the vibrational dynamics and the thermal conductivity is investigated in Sec. V. An extension of the phonon gas model to high frequencies is discussed and applied to the computation of the mode diffusivity. Finally our conclusions are summarized in Sec. VI.

II. EXPERIMENT

The inelastic neutron and x-ray scattering techniques represent two complementary probes of the vibrational dynamics. In the case of vitreous silica, both IXS and INS give access to the dynamic structure factor $S(q,\omega)$, since Si and O atoms have negligible incoherent neutron-scattering cross sections. The two techniques allow spanning of different $q-\omega$ space regions, which can be chosen so as to partially overlap.

A. IXS experiment

1. Instrument setup

The IXS experiment was carried out at the inelastic x-ray scattering beamline ID16 of the European Synchrotron Radiation Facility in Grenoble, France. A high energy resolution of 2.8 meV is reached employing the (9,9,9) reflection of the silicon crystal monochromator. A backscattered beam of 17.794 keV energy is focused by a grazing incidence toroidal mirror on the sample position to a spot size of 150 (vertical) $\times$ 260 (horizontal) μm^2 full width at half maximum (FWHM). Spectra at five different momentum transfers are recorded simultaneously, exploiting the five crystal analyzer spectrometer arm. At the selected crystal reflection, the angular offset between two adjacent analyzers corresponds to a difference of 2.4 nm^{-1} in exchanged momentum. The energy scans are performed by varying the monochromator temperature with respect to that of the analyzer crystals, both controlled with a precision of ≈ 0.2 mK. Further details on the IXS setup can be found elsewhere.[41]

2. Sample environment

The sample used for the experiment is a disk-shaped Suprasil fused quartz sample purchased by Goodfellow, with a 2 mm diameter and a 1.4 mm thickness, chosen to match the photoelectric absorption length of vitreous silica at the used incident energy of 17.8 keV. The sample is placed in a cylindrical graphite holder of 5 mm diameter which presents two circular openings of 1 mm diameter along the beam path. The graphite holder is enclosed in a high-temperature vacuum chamber specifically designed for IXS experiments. The sample has been radiatively heated using an Ω-shaped graphite foil with a thickness of 100 μm and a surface of a few cm^2. The power needed to maintain the sample at 1570 K is around 700 W. The sample temperature is measured by means of two different thermocouples (types *B* and *S*) placed near the sample and near the heating element. The temperature has been measured and found to be stable during several days in a range of ± 10 K around the set point. The sample is polished with hydrofluoric acid before the experiment to reduce the risk of devitrification as suggested in the literature.[42]

3. Experiment and results

The dynamic structure factor is measured at the two temperatures $T = 1570$ K and $T = 920$ K. These values are chosen in order to span a wide temperature range from below to above the glass transition temperature, $T_g \sim 1450$ K.[43] The spectra are collected on the Stokes side in view of the necessity to cover a wide dynamical range, up to 100 meV, to properly observe the dispersion of the longitudinal excita-

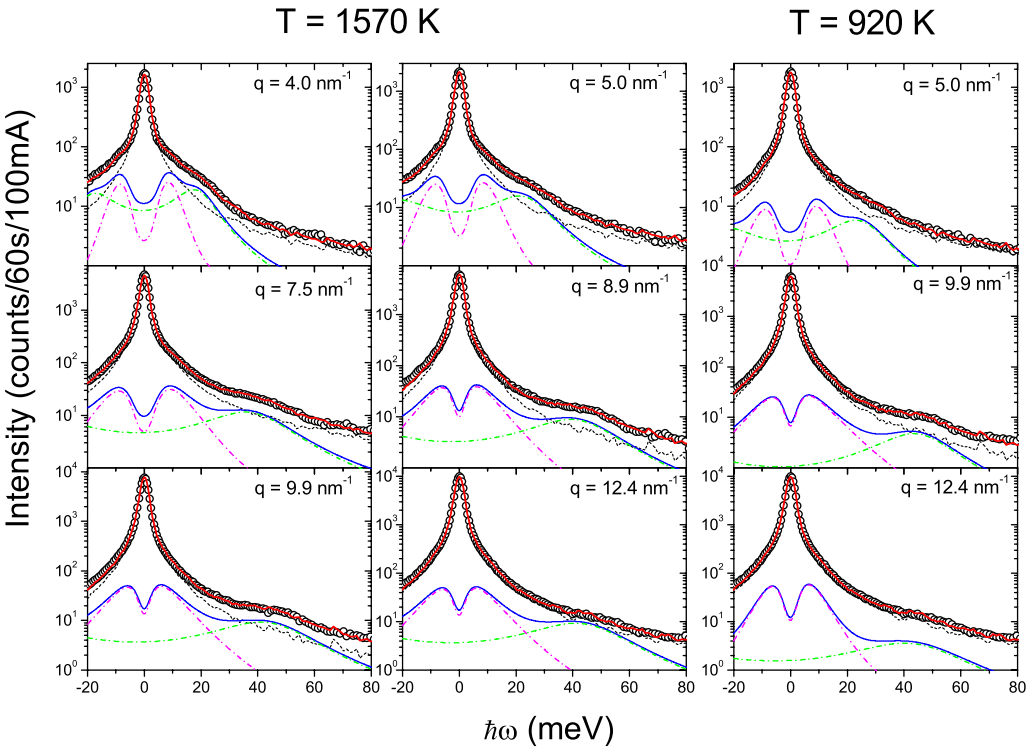

FIG. 1. (Color online) Selection of IXS spectra at the indicated exchanged wave vectors at the two measured temperatures. The spectra are plotted together with the best-fitting function (continuous line, red) and its main terms: the elastic line (dashed, black), the inelastic contribution (continuous, blue), and the two inelastic components (dashed-dotted, magenta and green). The baseline y_0 [see Eq. (3)] lies below the plotted window.

tions up to the border of the first pseudo-Brillouin zone. Only a small portion of the anti-Stokes part is measured to properly describe the elastic line. To achieve a good signal-to-noise ratio, each spectrum is collected with a long integration time of around 15 min per point. In particular the spectra are collected over an overall time of around 45 and 30 h at 920 and 1570 K, respectively. This long integration time is necessary because vitreous silica is characterized by a low inelastic-to-elastic-intensity ratio. Moreover, the visibility of the inelastic intensity on the longitudinal modes tends to become worse on increasing q because of the broadening of the excitations, often requiring even longer integration times. The sample did not present any trace of crystallization during the experiment. The absence of devitrification has been checked by measuring the static structure factor $S(q)$ at regular intervals during the experiment.

A selection of spectra at the two measured temperatures and at different wave vectors is shown in Fig. 1 in logarithmic scale in the intensity axis. The good signal-to-noise ratio can be appreciated by the smoothness of the points on the tail of the spectrum, where the count rate is on the order of a few counts per minute. The spectra in Fig. 1 are presented together with the instrumental response function and the best-fitting function, the details of which will be discussed in Sec. III B. Here we simply note that the inelastic part of the spectrum is characterized by the presence of two components. The first component is almost nondispersing and situated near the elastic line, while the second one presents a marked dispersion and is well detectable over the entire explored wave-vector range.

B. INS experiment and results

The neutron inelastic spectra were collected at the cold neutron time-of-flight spectrometer IN6 at the high-flux reactor of the Institut Laue-Langevin in Grenoble. The measurements are performed with an incoming neutron wavelength of 4.12 Å, corresponding to an energy $E_{\text{in}} = 4.82$ meV. The use of cold neutrons allows us to span the wave-vector region between 8 and 25 nm^{-1}, which overlaps with the one explored by IXS in the present experiment, with a high energy resolution of around 0.15 meV FWHM, about 20 times higher than that of the IXS experiment. The resulting spectra are, however, affected by a relatively small dynamical range between $-E_0$ and 30 meV, where the positive values are associated with the anti-Stokes side, with the Stokes side limited by the energy of the incoming neutrons. Measurements were carried out at the three temperatures $T = 15$, 50, and 300 K. The neutron data were then treated using the standard conversion of time of flight to energy and corrected for the aluminum empty cell signal. The detector efficiency was corrected by using a vanadium sample as reference. The sample used in the experiment was a Suprasil v-SiO_2 disk of 5 cm diameter and 4 mm width, in order to match the neutron-beam size and to minimize the multiple-scattering contribution to the spectra.

A selection of spectra obtained at room temperature in the explored wave-vector region is plotted in Fig. 2. The data are presented together with the best-fitting functions, which will be described in Sec. III B. The high resolution of the time-of-flight technique with cold neutrons is apparent from the

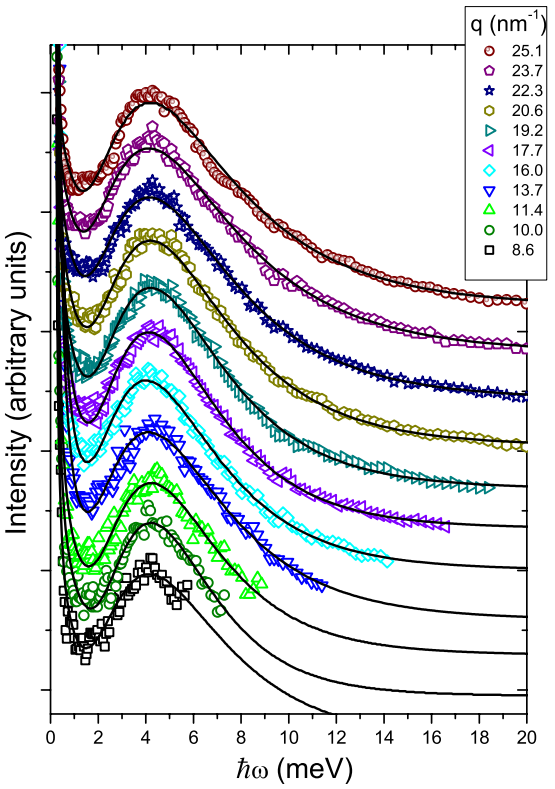

FIG. 2. (Color online) Selection of INS spectra at the indicated exchanged wave vectors at room temperature. The spectra are plotted together with the best-fitting function. Due to the kinematic constraints of the cold-neutron-scattering technique, the spectra are presented on the anti-Stokes side only. The frequency scale has thus the opposite sign compared to the IXS spectra.

sharp elastic peak of Gaussian shape. Here we observe that these spectra are characterized by a well defined nondispersing single component which is located at the Boson peak frequency.[44] Based on direct visual inspection of the IXS and INS spectra, it appears that the peak observed in the neutron data is located at the same frequency as the nondispersing component in the IXS measurement. The other component that is apparent in the IXS spectra and disperses with increasing q is outside the dynamical range of the neutron technique. A neutron experiment performed in a similar frequency-wave-vector space region was reported in Ref. 12 and compared to an early IXS experiment. The presence of two components was not revealed there because of the lower statistical accuracy of that early IXS measurement and because of the low wave-vector region ($q<4$ nm^{-1}) explored with the IXS probe in Ref. 12.

III. DATA ANALYSIS

A. Theoretical background

The main quantity describing the dynamics as a function of time is the normalized autocorrelation function of the density fluctuations,

$$\phi_q(t) = \frac{1}{S(q)}\langle \delta\rho_q^*(0)\,\delta\rho_q(t)\rangle,$$

where $S(q)=\langle|\delta\rho_q|^2\rangle$ is the static structure factor and $\delta\rho_q(t)=\Sigma_l e^{i\vec{q}\cdot\vec{r}_l(t)}/\sqrt{N}$ is the density fluctuation of wave vector $\vec{q}$. The dynamic structure factor is defined as the time Fourier transform of the density correlator,

$$S(q,\omega) = S(q)\int_{-\infty}^{\infty} dt e^{i\omega t}\phi_q(t).$$

In the harmonic approximation, the particles vibrate around the arrested glassy configuration defined by the positions $\vec{x}_l$. In terms of the eigenvectors $\vec{\phi}_l^m$ of the dynamical matrix $\hat{M}$, the one-phonon contribution to the dynamic structure factor can be written as[7]

$$S^{(1)}(q,\omega) = \hbar|n(\omega)+1|\sum_m |Q_m|^2\delta(\omega^2-\omega_m^2),$$

$$Q_m = \frac{1}{\sqrt{N}}\vec{q}\cdot\sum_l \frac{\vec{\phi}_l^m}{\sqrt{m_l}}e^{i\vec{q}\cdot\vec{x}_l}e^{-W_l}, \quad (1)$$

where $n(\omega,T)$ is the Bose population factor for phonons of energy $\hbar\omega$ at temperature T, ω_m^2 is the mth eigenvalue, and m_l is the mass of atom l. The Debye-Waller exponent $W_l=\frac{1}{2}\langle(\vec{q}\cdot\vec{u}_l)^2\rangle$ is a function of the displacement $\vec{u}_l$ of atom l from its equilibrium position.

The one-phonon term $S^{(1)}(q,\omega)$ can be written as a function of the imaginary part of the phonon propagator $\hat{G}(\omega)=(\omega^2-\hat{M})^{-1}$ in the momentum representation.[45,46] The propagator is then conveniently expressed in terms of the complex self-energy $\Sigma_q(\omega)=\Sigma_q'(\omega)+i\Sigma_q''(\omega)$, resulting in the following inelastic dynamic structure factor:

$$S_{\rm cl}^{(1)}(q,\omega) = -\frac{k_BTq^2}{\pi m\omega}e^{-2W(q)}\,{\rm Im}[\omega^2-v^2q^2+\Sigma_q(\omega)]^{-1}, \quad (2)$$

where k_B is the Boltzmann constant and v is the macroscopic speed of sound. The subscript "cl" indicates the classical limit $k_BT\gg\hbar\omega$, used to approximate the population factor for phonons. The Debye-Waller factor is reduced here to the expression commonly used for disordered systems, where $W(q,T)\sim q^2\langle u^2(T)\rangle/6$. It should be remarked that this expression is strictly valid only for a monoatomic system of particles with mass m.

The use of the self-energy is convenient because different approximations can be developed in terms of this quantity.[47–49] Moreover, the real and imaginary parts of the self-energy in the wave-vector representation have a direct physical interpretation. The real part describes the shift of the peak position with respect to the bare long-wavelength acoustic dispersion and the imaginary part, the peak broadening. Both of these effects are induced by the disorder of the glass structure.

B. Fitting procedure

The dynamic structure factor obtained in the previously described theoretical framework is a classical model. The

quantum nature of the interaction of radiation with matter reveals itself as an asymmetry between the Stokes and anti-Stokes sides of the spectra, as dictated by the principle of detailed balance. The measured intensity can be expressed in terms of the classical $S_{\mathrm{cl}}(q,\omega)$ as

$$I(q,\omega) = y_0 + I_0 R(\omega) \otimes S_{\mathrm{cl}}(q,\omega)\frac{\hbar\omega}{k_B T}[n(\omega,T)+1]. \quad (3)$$

Here the model for the dynamic structure factor is convoluted to the instrumental resolution function $R(\omega)$ and multiplied to the Bose population factor $n(\omega,T)$. The baseline y_0 is added in order to take into account the electronic background of the detector and the environmental background. The overall intensity factor I_0 is a function of the wave vector q and depends on many factors. In the IXS measurement it is influenced by the atomic form factors, the efficiency of the analyzers, and by all other angle-dependent instrumental correction factors. In the case of neutrons, it is mainly affected by the detector efficiency and by the scattering geometry. In principle one could normalize the spectra to a reference scatterer, such as vanadium for neutrons. However it is more straightforward to normalize the spectra to the known static structure factor $S(q)$, using the x-ray[50] and neutron-diffraction[51] data to respectively scale the IXS and INS measurements.

As shown in Fig. 1, the IXS spectra are characterized by a double peak structure. The analysis is performed by fitting the measured spectra to a two-component model in order to extract the main parameters such as the positions, widths, and intensities of the peaks. A formal derivation of the line shape from the theoretical approach previously described would require the development of some proper approximations for the complex self-energy in Eq. (2) in order to retrieve the two-component structure in the dynamic structure factor. We have chosen to follow a simpler approach which consists of describing the inelastic component of the $S_{\mathrm{cl}}(q,\omega)$ as the sum of two phenomenological functions, the choice of which is based on qualitative arguments.

The choice of the function used to describe the shape of the nondispersing peak observed in both the IXS and the INS measurements is dictated by the shape of the neutron spectra, where this feature is observed with a good signal-to-noise ratio as shown in Fig. 2. This peak is almost constant as a function of the wave vector and it has the shape of the boson peak observed in $g(\omega)/\omega^2$, where $g(\omega)$ is the effective neutron density of states.[44] The shape of the boson peak is usually described[52] by means of a logarithmic-normal function. The higher-frequency propagating mode visible in the IXS measurement can be associated with the longitudinal-acoustic mode[13] and can be described by a damped harmonic oscillator (DHO) model. The validity of this model in describing the IXS spectra of vitreous silica has been checked by studying both the frequency[13,14,53] and the wave-vector[54] dependences of the scattering function.

The dynamic structure factor in Eq. (3) is thus modeled by the following function:

$$S_{\mathrm{cl}}(q,\omega) = A_{\mathrm{el}}(q)\delta(\omega) + A_1(q)\frac{\mathcal{N}}{\omega^2}\exp\left(-\frac{\ln^2[|\omega|/\Omega_1(q)]}{2\sigma^2(q)}\right) + A_2(q)\frac{1}{\pi}\frac{\Omega_2^2(q)\Gamma(q)}{[\omega^2-\Omega_2^2(q)]^2+\omega^2\Gamma^2(q)}, \quad (4)$$

where the subscripts 1 and 2 refers to the lower-frequency nondispersive component and to the higher-frequency dispersive one, respectively. The constant $\mathcal{N}=\frac{\Omega_1(q)}{2\sqrt{2\pi\sigma^2(q)}}\exp[-\frac{\sigma^2(q)}{2}]$ is a normalization factor. The resulting model for the measured intensity in Eq. (3) is defined by eight parameters: the baseline y_0; A_{el}, which is the intensity of the elastic line; A_1, Ω_1, and σ, which describe the lower-frequency component; and A_2, Ω_2, and Γ, which are the intensity, position, and width of the dispersing excitation. The best-fitting parameters are estimated from the measured spectra by means of a minimization routine designed to find the minimum of the χ^2 in the parameter space. The resulting line shapes for the IXS experiment are presented in Fig. 1 for a selection of wave-vector values at the two measured temperatures.

In the INS spectra presented in Fig. 2, the higher-frequency mode lies outside the available dynamical range. In this case the model for $S_{\mathrm{cl}}(q,\omega)$ does not include the DHO function. It has been necessary however to include a further contribution to the spectrum in the form of a Lorentzian line peaked at zero frequency. The fitting procedure gives for this term a full width at half maximum on the order of 3.5 meV. This term describes the presence of a quasielastic contribution in the spectrum, which is visible in Fig. 2 as a weak broadening of the elastic line. This contribution cannot be assigned to the resolution function alone, which is an almost perfect Gaussian as confirmed by the measurement on vanadium. The fact that this contribution is not a spurious instrumental effect is confirmed by the low-temperature measurement at 15 K. At this temperature there is no signature of a broadening of the elastic line apart from the almost perfect Gaussian instrumental resolution function. The nature of the quasielastic scattering in silica glass has been widely studied by means of both Raman[55] and neutron[56] scattering. This aspect of the dynamics is however outside the scope of the present work and will not be further investigated here. The best-fitted line shapes to the INS spectra are presented in Fig. 2, where the good agreement between the data and the fitting function can be appreciated over the entire explored energy–wave-vector range.

Because of the wide Lorentzian-type elastic peak which dominates the IXS spectra in Fig. 1, the inelastic features of the spectrum are better appreciated by subtracting the elastic line once its intensity A_{el} is determined through the fitting procedure. A selection of IXS inelastic spectra is presented in Fig. 3, where the wave-vector evolution of the two inelastic components is shown at the highest measured temperature of 1570 K. The inelastic intensity (left spectra), in absolute units, is compared to the inelastic longitudinal current $\frac{\omega^2}{q^2}I_{\mathrm{inel}}$ (Ref. 57) (right spectra). The lower-frequency inelastic component is better appreciated in the plots of $I_{\mathrm{inel}}(q,\omega)$, while the longitudinal mode is enhanced in $C_{\mathrm{inel}}(q,\hbar\omega)$ by the ω^2 factor.

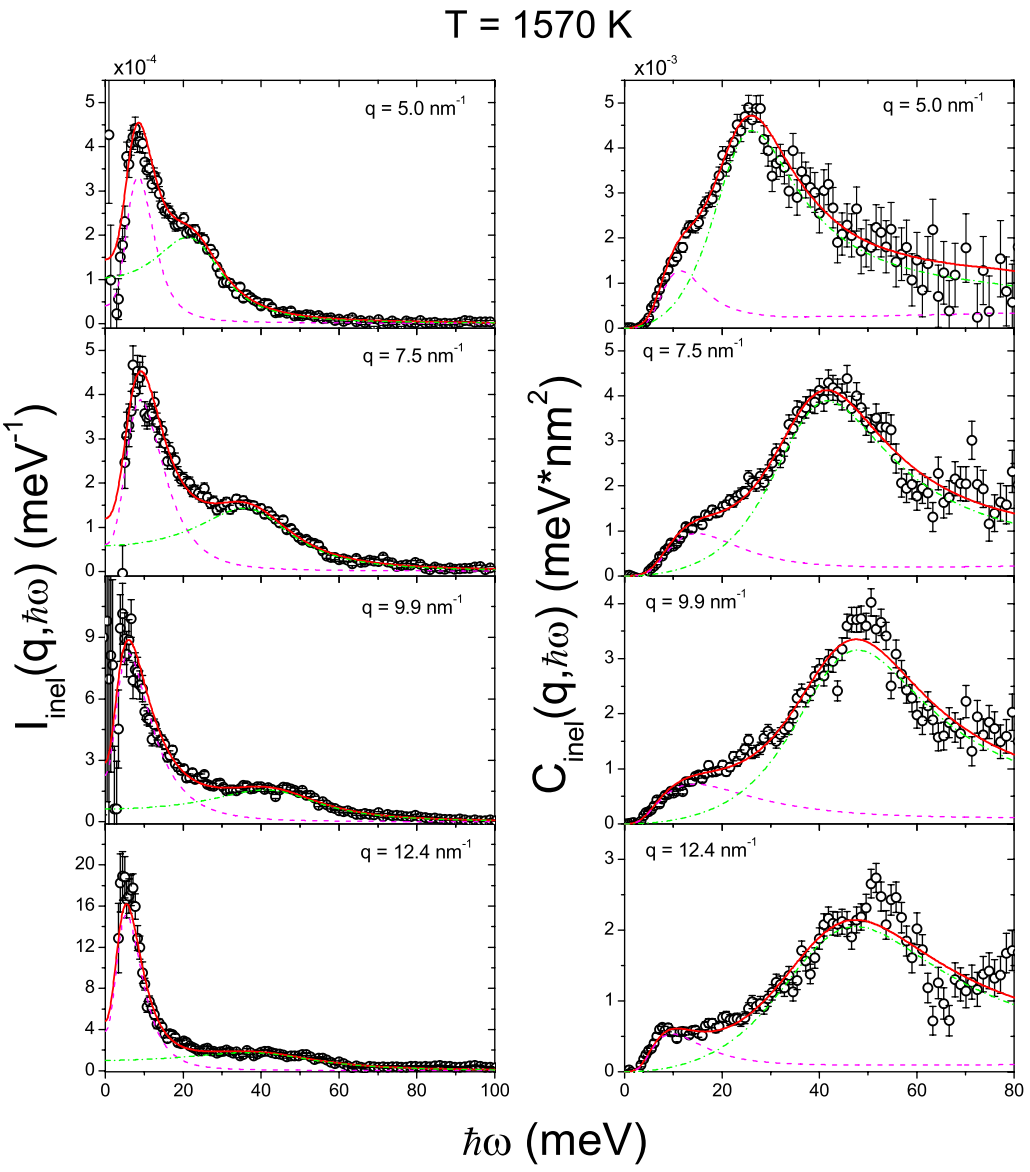

FIG. 3. (Color online) Inelastic part of the IXS spectra at selected exchanged wave vectors. In the left panel the spectra are plotted as $I_{\mathrm{inel}}(q,\hbar\omega)$ and compared to the two-component best-fitting function (continuous line, red). The left panel shows the same spectra plotted as longitudinal inelastic current $C_{\mathrm{inel}}(q,\hbar\omega)$ (Ref. 57) to emphasize the dispersion of the longitudinal mode. The two inelastic contributions are plotted as dashed (magenta) and dashed-dotted (green) lines. The error bars are $\pm\sigma$ standard deviations computed taking into account both the experimental errors on the spectra and the resolution and the standard deviation on the parameter A_{el} as determined from the fit. The spectra are normalized to absolute units using the known values for the static structure factor (Ref. 50).

IV. VIBRATIONAL DYNAMICS AT TERAHERTZ FREQUENCIES

A. Dispersion relation and density of states

The presence of reasonably well defined peaks in the dynamic structure factor suggests that, even in the glassy state at THz frequencies, a dispersion curve can still be meaningfully defined. If the peak position $\Omega(q)$ is plotted as a function of the wave vector at which the spectrum is measured, the dispersion curve presented in Fig. 4 is obtained. Here the two components measured by IXS in the temperature range between 920 and 1570 K are presented and compared to the peak position observed in the INS measurements at room temperature. The results of previous experiments are also plotted for comparison.[13,53] In the wave-vector region above 4 nm^{-1}, only one experiment was performed in the past[14] at the temperature $T=1270$ K (open and filled circles in the figure). The dispersion curve allows us to identify three distinct wave-vector regions:

(i) A small wave-vector region, $q<4$ nm^{-1}, where a single excitation model well describes the measured $S(q,\omega)$. This mode is characterized by a sound velocity compatible with the macroscopic longitudinal sound speed, which, in the range of temperatures of interest here, has been measured by Brillouin light scattering[29] to be about 6400 m/s (the lines in Fig. 4 correspond to the values of sound velocity at the three temperatures of 920, 1270, and 1570 K).

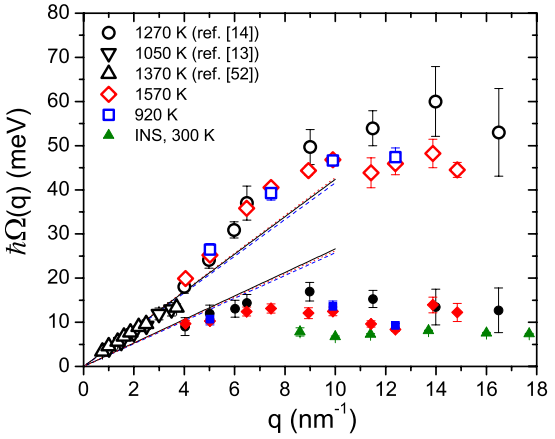

FIG. 4. (Color online) Dispersion relation for v-SiO_2 in the first pseudo-Brillouin zone from the IXS and INS data. Open (longitudinal branch) and filled (transverse-optic-like component) diamonds: present work, $T=1570$ K (red); open and filled squares: present work, $T=920$ K (blue); open and filled circles: Ref. 14, $T=1270$ K; up triangles: Ref. 53, $T=1375$ K; down triangles: Ref. 13, $T=1050$ K. The position of the peak in the INS spectra is reported as filled triangles (green). The parameter Ω_i with $i=1,2$ in Eq. (4) is the position of the peaks in the current correlation function, thus slightly higher than the corresponding peak positions in $S(q,\omega)$. The lines correspond to the macroscopic sound velocity measured by Brillouin light scattering (Ref. 29) for the longitudinal and transverse excitations: $v_l=6320$ m/s and $v_t=3910$ m/s at $T=920$ K (dashed blue), $v_l=6440$ m/s and $v_t=4040$ m/s at $T=1270$ K (filled black), $v_l=6500$ m/s and $v_t=3980$ m/s at $T=1570$ K (dotted red).

(ii) An intermediate wave-vector region, $4<q<10$ nm^{-1}, where the apparent sound velocity of the longitudinal peak speeds up to a value between 8000 and 9000 m/s.

(iii) At still higher wave vectors, the dispersion curve of the longitudinal mode tends to saturate at a value of around 50 meV.

Concerning the lower-frequency feature, which appears in both the IXS and the INS spectra, it is almost nondispersing and located at a frequency of around 8–10 meV. It is worth noting that the Ω_i parameters of the model function in Eq. (4) measure the position of the peaks in the current $C(q,\omega)$. These are shifted to higher energies when compared to the peaks in $S(q,\omega)$ if the peak width is comparable to its position. The peak observed by means of neutron scattering is, in fact, located around the energy of the boson peak, which is on the order of 4.2 meV, as it can be seen from Fig. 2. The position of this lower-frequency feature in the IXS spectra appears to be slightly higher than the one detected by INS. This discrepancy is more likely due to a systematic error induced by the strong Lorentzian-type elastic peak which mixes with the low-frequency component in the IXS experiment, as apparent from Fig. 1. The difference in shape between the IXS and INS spectra may also be due to the difference between the atomic form factors and the neutron-scattering lengths, which respectively weight the scattering cross section in the IXS and INS experiment.

The comparison with the results of molecular-dynamics simulations of vitreous silica[14,19,20,22] suggests the interpretation of this lower-frequency feature as the high-frequency evolution of the transverse-acoustic mode. It appears in the longitudinal spectrum because of the ill definition of its polarization at high wave vectors in a disordered medium.[58] The results of MD simulations[19] indicate that the mode merges in an opticlike branch reminiscent of the corresponding optic branch of crystalline quartz. In fact, cristobalite presents a marked peak in the INS spectra located around the position of the boson peak in vitreous silica.[59] This peak in cristobalite results in part from the flattening of the transverse-acoustic modes and is in part due to the presence of an optical mode in the same energy region.[59,60] The peculiar wave-vector dependence of the $S(q,\omega)$ in the boson peak region was interpreted by Buchenau *et al.*[8] in terms of librations and rotations of coupled SiO_4 tetrahedral units. The optical character of the boson peak modes is indicated also in hyper-Raman experiments.[61]

In the following we will use the terms "longitudinal" and "transverse-optic" to label the high- and low-frequency features appearing in the $S(q,\omega)$. This notation shall not be taken as descriptive of their nature, since the polarization character becomes less and less defined as the wave vector is increased.

The marked positive dispersion of the longitudinal mode which sets in for $q\sim 4$ nm^{-1} is not affected by temperature in the temperature range investigated here. This confirms the interpretation of this effect as resulting from the structural disorder of the glass and not from anharmonic processes. Because of disorder, the eigenvectors of the dynamical matrix are not simple plane waves as in the case of crystals. In other terms the wave vector q cannot be properly used to label the normal modes. In the Green's function approach in Eq. (2), this is reflected in the presence of a non-negligible complex self-energy $\Sigma_q(\omega)$. The structural disorder induces a broadening of the peak and a shift with respect to the long-wavelength acoustic linear dispersion, which is reflected in the real part of the self-energy $\Sigma'_q(\omega)$.

The possibility of assigning an average wave vector q to the mode of frequency $\Omega(q)$ becomes less and less justified as the wave vector is increased. Above 10 nm^{-1} the concept of a dispersion curve and the description of the peaks in the dynamic structure factor as modes or excitations seem heavily questionable. This is better seen by comparing the dynamic structure factor determined by IXS with the effective density of vibrational states $g(\omega)$ determined by means of INS.[7,8,10] The effective density of states is obtained in a coherent neutron-scattering experiment by averaging the measured dynamic structure factor over a large wave-vector range and applying the incoherent approximation.[7] The comparison with the IXS spectra can therefore be conveniently performed by recasting the inelastic part of $S(q,\omega)$ in terms of $g(q,\omega)$, the function which converges to the density of states in the high q limit[7] as follows:

$$S_{\mathrm{cl}}^{\mathrm{inel}}(q,\omega)=e^{-2W(q)}\frac{k_BTq^2}{2\tilde{m}\omega^2}g(q,\omega), \tag{5}$$

where $S_{\mathrm{cl}}(q,\omega)=S(q,\omega)k_BT/\hbar\omega[n(\omega,T)+1]^{-1}$ denotes the dynamic structure factor in the classical limit and the average

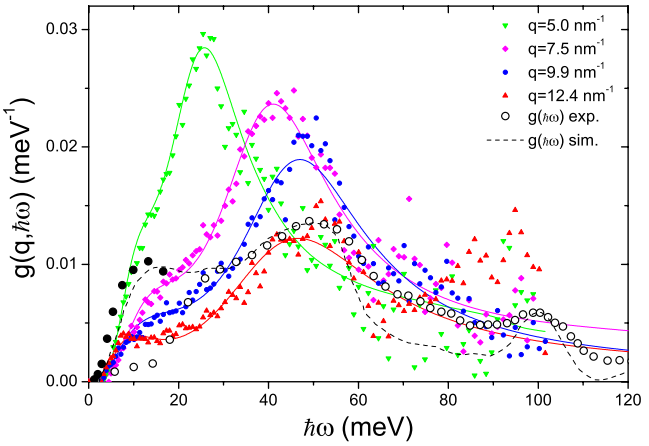

FIG. 5. (Color online) Evolution of $g(q,\omega)$, measured using IXS at $T=1570$ K and computed by using Eq. (5), compared to the neutron effective density of vibrational states $g(\omega)$. $g(q,\omega)$ is plotted at the four indicated q values. The $g(\omega)$ curves are from two literature measurements (Refs. 7 and 8) (open and filled dots) and a recent *ab initio* simulation (Ref. 23) (dashed line) and are normalized to unity. The $g(\omega)$ from the experiment of Carpenter and Price (Ref. 7) seems to be not reliable in the boson peak region because a large spectral range around the elastic peak has been neglected.

mass is approximated to $\tilde{m}^{-1}=\Sigma_l m_l^{-1}/N$. The comparison between $g(q,\omega)$ determined from the IXS data and the effective neutron density of states $g(\omega)$ is shown in Fig. 5. The Debye-Waller factor has been estimated using literature values of the mean-square atomic displacement,[21] which has a value of $\sqrt{\langle u^2\rangle}\sim 0.2$ Å at room temperature.

For a wave vector on the order of 12 nm^{-1}, the longitudinal peak is seen to already merge with the 50 meV peak of the density of states. This observation demonstrates that at these wave vectors the dynamic structure factor has almost completely lost its coherence content, giving information similar to the one present in $g(\omega)$. The other peak in the density of states around 10 meV corresponds to the excess of modes at the boson peak.

B. Integrated intensity of the modes

A deeper insight into the nature of the two inelastic components appearing in the spectrum can be obtained by looking at their integrated intensities. The one-phonon harmonic approximation for $S(q,\omega)$ introduced in Eq. (1) can be used to estimate the intensity of the mode as a function of wave vector. If the eigenvectors can be treated as plane waves $\vec{\phi}_l^m=\hat{\sigma}\cdot e^{-i\vec{q}_m\cdot\vec{x}_l}/\sqrt{N}$ of polarization $\hat{\sigma}$, the intensity is

$$I(q)=\int_{-\infty}^{+\infty} d\omega S_{\mathrm{cl}}^{(1)}(q,\omega)=|\hat{q}\cdot\hat{\sigma}|^2\frac{k_B T q^2}{m\omega^2(q)}e^{-2W(q)}, \qquad (6)$$

where the Bose population factor is estimated in the classical limit to compare to the intensity parameters obtained from the fitting model in Eq. (3). This relation shows that an acoustic mode with a linear dispersion is expected to have an integrated intensity constant with q.

In Fig. 6 the normalized intensity of the longitudinal mode is multiplied by the factor $\hbar^2\Omega^2(q)/q^2$, in order to get

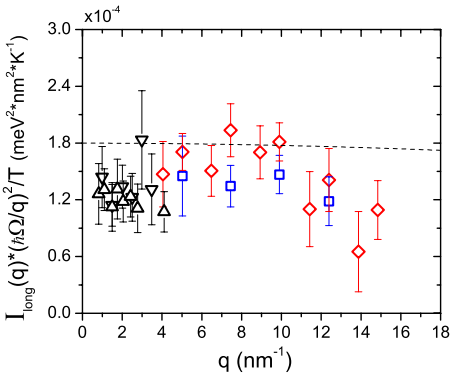

FIG. 6. (Color online) Integrated intensity of the longitudinal mode divided by temperature from the IXS data. The intensity is multiplied by the factor $\hbar^2\Omega^2(q)/q^2$ to take into account the positive dispersion effect. The dashed line is the quantity $\hbar^2 k_B/m$ times the Debye-Waller factor as from Eq. (6). Symbols are the same as in Fig. 4. The integrated intensity of the longitudinal mode is obtained in absolute units as $I_{\mathrm{long}}=S(q)A_2/A_{\mathrm{tot}}$, where $A_{\mathrm{tot}}=A_{\mathrm{el}}+A_1+A_2$ is the total area of the fitting model in Eq. (4).

rid of the effect of the positive dispersion. This is an estimate of the intensity of the longitudinal mode in the current correlation function $C(q,\omega)$, which can be directly compared to $e^{-2W(q)}\hbar^2 k_B/m$. This curve is presented as a dashed line in the figure, with m defined as an average mass, $m=\Sigma_l m_l/N$. To perform this comparison in absolute units, we have carefully checked the low wave-vector values of the dynamic structure factor $S(q)$ measured with small-angle x-ray scattering by different authors.[50] The line is seen to overestimate by 25% the measured intensity at low q, where the plane-wave approximation is supposed to work. This discrepancy can be attributed to the fact that the model is strictly valid only for a monoatomic system. A further source of discrepancy can come from the definition of the $S(q)$, which is derived from the diffracted intensity treating the scattering form factors in the incoherent approximation.[50]

In Fig. 7 the integrated intensity I_{tr} of the transverse-optic peak, in both IXS and INS spectra, is plotted in absolute units and compared to the q dependence of the $S(q,\omega)$ measured by Buchenau *et al.*[8] for frequencies on the order of 1 THz, around the position of the boson peak. The agreement between the integrated intensity and the q dependence of the $S(q,\omega)$ confirms that at the boson peak (BP) frequency, the dynamic structure factor is dominated by the transverse-optic peak. The continuous line in the figure is the prediction of Eq. (6) evaluated at the boson peak frequency $\omega=\omega_{\mathrm{BP}}$ and multiplied by a normalizing constant which, at least at low wave vectors, describes the fraction of the transverse-optic mode polarized along the longitudinal direction. The inelastic intensity measured by neutrons at room temperature is comparable to the one detected by IXS at much higher temperatures. The cross section of the transverse-optic peak is thus higher in INS by a factor on the order of 4, with the intensity proportional to temperature. This observation suggests that the measurement of the transverse-optic mode is differently weighted in the cross sections of neutrons and x rays. Because the atomic form factor is proportional to the number of electrons, IXS is more sensible to silicon atoms.

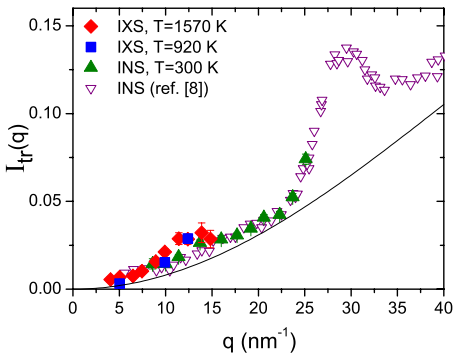

FIG. 7. (Color online) Inelastic intensity of the transverse-optic peak as a function of the exchanged wave vector [$I_{tr}=S(q)A_1/A_{tot}$ in Eq. (4)]. Diamonds (red): IXS, $T=1570$ K; squares (blue): IXS, $T=920$ K; filled triangles (green): INS, $T=300$ K. The open triangles (purple) correspond to the wave-vector dependence of the dynamic structure factor as measured by INS in Ref. 8. These points are arbitrarily rescaled on the present work data. The line is the behavior of Eq. (6) for a nondispersive excitation as discussed in the text.

On the contrary, the INS cross section is dominated by the oxygen contribution.

The peak in I_{tr} located at about 30 nm^{-1} is not reproduced by the simple plane-wave model in Eq. (6). This failure of the plane-wave description of the boson peak has been widely investigated in the past and is at the base of the tetrahedral model of Buchenau *et al.*[8] For relatively small wave vectors however, Eq. (6) can still be used to determine the q dependence of the ratio between the nondispersing and the dispersing peaks. This ratio is plotted in Fig. 8 in log-log scale together with the best-fitted q^2 slope. This momentum dependence is eventually expected to be violated in the very low wave-vector region if the nondispersive peak gets purely transverse. This lower region however lies at lower q's than those explored in the present experiment. The figure illustrates the reason why the lower-frequency peak is very difficult to detect for $q<4$ nm^{-1}, the spectrum being dominated by the longitudinal mode in the low wave-vector region probed here.

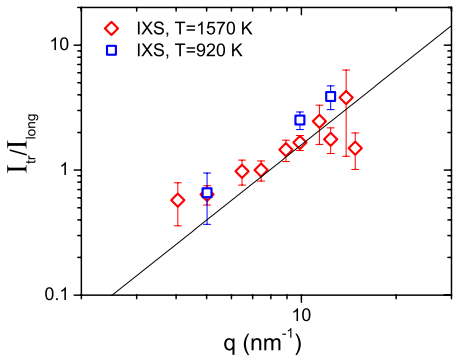

FIG. 8. (Color online) Ratio of the transverse-optic intensity to the longitudinal integrated intensity as a function of the exchanged wave vector in log-log scale at the two measured temperatures. The line is the best-fitted q^2 slope, suggested by Eq. (6).

V. THERMAL CONDUCTIVITY

The peculiar temperature dependence of the thermal conductivity of glasses has been the subject of many investigations both from the experimental and the theoretical sides. In dielectric glasses at low temperatures, heat is carried by acoustic excitations, whose mean free path can be determined by means of spectroscopic[4,15,16] or acoustic[3,5,9] measurements. Three temperature ranges can be identified, where different sound damping mechanisms dominate the sound attenuation process. In the low-temperature range, $T<1$ K, the thermal conductivity is quadratic with respect to temperature and the sound damping is governed by tunneling two level systems.[6] For temperatures around 10 K, the conductivity shows a plateau, whose nature has been strongly debated in the literature[1,62–64] and is still an open issue.[39,65–67] Then, around 30 K, the thermal conductivity rises again above the plateau.[33,35] We will be mainly concerned here with this high-temperature range. The IXS technique is, in fact, limited to $q>1$ nm^{-1}, which in v-SiO_2 corresponds to energies above 4 meV as shown in Fig. 4. Using the dominant phonon approximation,[68,69] this energy range corresponds to temperatures above 10 K.

A. Mean free path of the high-frequency modes

The mean free path ℓ of an acousticlike mode can be estimated from the damping parameter Γ of the DHO function in Eq. (4), through the relation[70] $\ell=\omega/(q\Gamma)=v/\Gamma$. The wave-vector dependence of the longitudinal damping Γ and of the corresponding energy mean free path is plotted in the upper and lower panels of Fig. 9, respectively. The present investigation confirms the temperature independence of the sound attenuation in this high-frequency range.[71] The damping $\Gamma(q)$ is seen to deviate from the low wave-vector q^2 behavior for $q\geq 4$ nm^{-1}. The longitudinal mean free path is estimated assuming a constant speed of sound $v\sim 6000$ m/s, neglecting the positive dispersion and the saturation of $\Omega(q)$ at high wave vectors.

In order to use the measured sound attenuation to estimate the thermal conductivity, the wave-vector dependence of Γ is fitted to the following phenomenological function:

$$\Gamma(q)=D\frac{q^{\eta_1}}{[1+(q_c/q)^{(\eta_2-\eta_1)\delta}]^{1/\delta}}. \quad (7)$$

This function describes a transition from a low q power law of exponent η_1 to a high q one with exponent η_2. The change in slope takes place around q_c and the parameter δ rules the sharpness of the transition between the two regimes. The parameters best fitted to the entire set of IXS data are reported in the caption of Fig. 9; they give the continuous curve shown in the upper panel. The curve $\ell=\lambda/2$ is also shown for comparison. In contrast to the common assumption[33,35,36,62,63] that the mean free path should saturate at the value indicated by the Ioffe-Regel criterion (defined either as $\ell\sim\lambda$ or $\ell\sim\lambda/2$), the measured ℓ is observed to decrease even further and to saturate at a value on the order of the interatomic spacing.

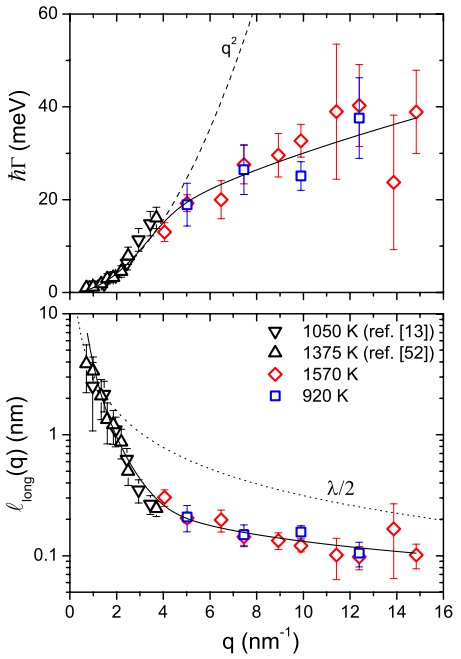

FIG. 9. (Color online) Upper panel: wave-vector dependence of the width parameter $\Gamma(q)$ of the longitudinal mode as determined by the fit of the IXS data to the model in Eq. (4) ($\Gamma\sim$ FWHM at low q). The dashed line is the q^2 law describing the low wave-vector region. The continuous line is the best-fitted curve to the function in Eq. (7), with the parameters $\eta_1=0.58$, $\eta_2=2.1$, $A=8$, $q_c=4$, and $\delta=4.5$. Symbols are the same as in Fig. 4. Lower panel: the energy mean free path computed as $\ell(q)=v/\Gamma(q)$, where a constant sound velocity $v=6000$ m/s is used. The continuous line is the curve of Eq. (7) and the dotted line is the $\ell=\lambda/2$ behavior. Symbols are the same as in Fig. 4.

B. Theory of the thermal conductivity in disordered systems

The thermal Kubo formula relates the thermal conductivity to the correlation function of the heat current operator $\hat{S}(t)$. A detailed derivation of the relevant expressions can be found in a review by Allen and Feldmann.[40] Here we will simply recall the main results that allow a computation of the thermal conductivity from the experimental data. Applying the harmonic approximation, the thermal conductivity can be expressed in terms of the mode diffusivity $D(\omega)$ as

$$k(T)=\frac{3N}{V}\int_0^\infty d\omega C(\omega/T)g(\omega)D(\omega), \tag{8}$$

where $C(\omega/T)=k_B x^2 e^x/(e^x-1)^2$, with $x=\hbar\omega/(k_B T)$, is the specific heat of an oscillator of energy $\hbar\omega$ and the vibrational density of states $g(\omega)$ is normalized to unity. The mode diffusivity is a function of the heat current operator $\hat{S}$ and of the resolvent $\hat{G}(\omega)=(\omega^2-\hat{M})^{-1}$ of the dynamical matrix $\hat{M}$,[72,73]

$$D(\omega)=\frac{4}{3\hbar^2\pi g(\omega)}\mathrm{Tr}\{\hat{S}\cdot\mathrm{Im}[\hat{G}(\omega)]\cdot\hat{S}\cdot\mathrm{Im}[\hat{G}(\omega)]\}.$$

Here Tr denotes the trace of the operator enclosed in brackets. In a crystal with mass disorder, Flicker and Leath[72] showed that in the framework of the coherent-potential approximation, the trace can be computed on the wave vectors basis. Writing the sum over the wave vectors as an integral over the frequency, the resulting mode diffusivity reads

$$D(\omega)=\frac{4v^2}{3\pi g(\omega)}\times\int_0^\infty d\omega'\frac{\omega'^2 g(\omega')[\Sigma''(\omega,\omega')]^2}{\{[\omega^2-\omega'^2-\Sigma'(\omega,\omega')]^2+[\Sigma''(\omega,\omega')]^2\}^2}. \tag{9}$$

Here the phonon propagator $G(\omega)$ is given in terms of the self-energy $\Sigma(\omega,\omega'(q))=\Sigma_q(\omega)$, defined in Sec. III A, and the prime and double primes denote its real and imaginary parts, respectively. The expression for the thermal conductivity resulting from Eqs. (8) and (9) represents an extension of the phonon gas model in the Peierls-Boltzmann theory.[74] This can be seen by taking the limit $\Sigma\to 0$ and assuming that the self-energy does not depend on ω'. Then computing the integral over ω' in the complex plane, the diffusivity reduces to

$$\lim_{\Sigma\to 0} D(\omega)=\frac{v^2\omega}{3\Sigma''(\omega)}=\frac{v\ell(\omega)}{3}, \tag{10}$$

where $\ell(\omega)$ is the energy mean free path of a phonon of energy $\hbar\omega$ as defined in Sec. V A. When inserted in Eq. (8), this result gives the usual thermal conductivity expression of the phonon gas model. It is worth noting that this limit is equivalent to the limit of small ω, where the density of vibrational states can be safely replaced by its Debye approximation.

Taking into account the results in Sec. III A, the thermal conductivity computed from the diffusivity of Eq. (9) is expressed as a double integral of a quantity which is proportional to the square of the inelastic part of the dynamic structure factor [see Eq. (2)]. This approach allows taking into account the broadening of the peak even when this is not negligible compared to the peak position.

The assumption that the heat current operator is diagonal at the wave-vector base is a strong approximation in the case of a structurally disordered glass. As discussed by Allen and Feldman,[40] in a topologically disordered system the operator $\hat{S}$ has non-negligible off-diagonal terms when computed on the dynamical matrix eigenstates basis. However the information that one can extract from the experiment is limited to the diagonal contribution in Eq. (9).

C. Thermal diffusivity

The evaluation of the thermal conductivity requires the knowledge of the sound attenuation of both the longitudinal- and the transverse-acoustic branches. The experimental data for the transverse modes are, however, limited to the ultrasound[3,6] and Brillouin light scattering (BLS) (Ref. 75) techniques. These data indicate that the internal friction parameter, defined as $Q^{-1}=\ell^{-1}\lambda/2\pi=\Gamma/\omega$, assumes roughly the same value for both the transverse and the longitudinal modes if taken at the same frequency. This result is confirmed by molecular-dynamics simulations[76] also in the high-

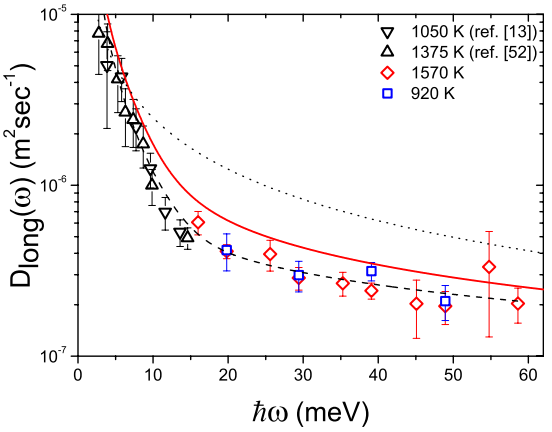

FIG. 10. (Color online) Diffusivity of the longitudinal mode as a function of frequency. The energy scale is limited by the longitudinal Debye frequency $\hbar v_L q_D \sim 62$ meV. The continuous (red) line is the result for $D(\omega)$ from Eq. (9), where $\Sigma(\omega,\omega'(q))=i\omega\Gamma(q)$. The dashed line is the value of the diffusivity expected from the phonon gas approximation in Eq. (10). The value used in Ref. 36 is also included for comparison as a dotted line and corresponds to the choice $\ell=\lambda/2$ in the phonon gas approach. Symbols are the same as in Fig. 4.

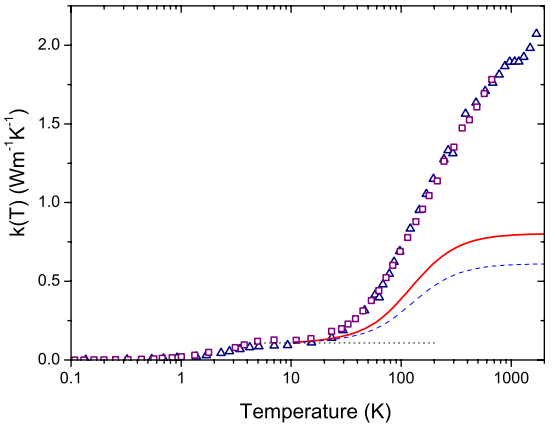

FIG. 11. (Color online) Thermal conductivity of vitreous silica. Squares (purple): from Ref. 36; triangles (navy): from Ref. 62. The continuous line (red) is the estimate from Eqs. (9) and (11). The phonon gas approximation in Eq. (10) is plotted for comparison as a dashed line (blue). The dotted line is the constant value added as an estimate of the plateau value and accounts for the omitted low-energy, $\hbar\omega < 3$ meV, contributions.

frequency region, where the attenuation is dominated by the structural disorder. Recast in terms of the mean free path, it implies $\ell_T/\ell_L = v_T/v_L$, where L and T denote the longitudinal and the transverse branches and v_L and v_T their sound velocities. In the following evaluation, we will thus assume that this ratio is constant at all frequencies. It is worth noting that the prediction of the soft potential model is in agreement with this assumption.[65]

Using the Debye approximation for the density of states, formula (8) for the thermal conductivity reduces to[77]

$$k(T) = \frac{3N}{V}\sum_{i=1}^{3}\int_0^{\omega_i} d\omega C(\omega/T)\frac{\omega^2}{\omega_i^3}D_i(\omega), \qquad (11)$$

where the sum is performed over the three acoustic branches. The Debye cut-off frequency $\omega_i = v_i q_D$ is the product of the mode sound velocity times the Debye wave vector $q_D = (6\pi^2 N/V)^{1/3}$, which is on the order of 15.8 nm^{-1} in v-SiO_2. The use of a different cut-off frequency for the longitudinal and the transverse modes allows us to give the same total weight to each mode in the density of states.

The diffusivity computed for the longitudinal mode, using Eq. (9) with $v = v_L$, is plotted in Fig. 10 as a continuous line. The self-energy in Eq. (9) is estimated from the damping of the longitudinal mode in the dynamic structure factor using $\Sigma_q(\omega) = i\omega\Gamma(q)$, the expression leading to the DHO fitting model in Eq. (4), discussed in Sec. III B. The wave-vector dependence of $\Gamma(q)$ is described by means of the function introduced in Eq. (7). The parameter Γ at a given frequency, thus not at the same q, is assumed to have the same value for the transverse and the longitudinal modes. Figure 10 shows also the diffusivity estimated directly from the Γ values using relation (10), valid in the phonon gas model. The use of the more general formula (9) gives a slightly higher diffusivity, which correctly converges for small frequencies to the value given by the phonon gas model. The diffusivity for the transverse mode is computed in the same way from Eq. (9) using the transverse speed of sound. The temperature and wave-vector dependences of the sound velocities are neglected in the present estimate and the zero temperature values $v_L = 6000$ m/s and $v_T = 3800$ m/s are used.[75]

D. High-temperature thermal conductivity

In the present evaluation of $k(T)$, the integral in Eq. (11) is computed in the energy region spanned by the IXS technique, above 3 meV in v-SiO_2 (see Fig. 4). This energy range corresponds to temperature lying above the characteristic plateau appearing in the thermal conductivity in the 1–10 K temperature range. The actual nature of the plateau is a source of debate in the literature[16,65–67] and lies outside the scope of the present work.

The thermal conductivity obtained from Eq. (11) is plotted in Fig. 11 and compared to the measured one. A constant value, the dotted line in the figure, is added to the computed thermal conductivity to account for the small contribution of lower-frequency attenuation mechanisms which give rise to the plateau. This contribution will eventually decrease at high temperatures but the error associated with the assumption of a constant term is small, less than 10%, with respect to the total $k(T)$. In the figure the prediction of the Kubo-type formula in Eq. (9) is compared to the one of the phonon gas model, in which the phonon mean free path is used to compute the diffusivity.

It is of some interest to compare the present result with a previous estimate by Cahill and Pohl.[36] They employed Eq. (11) using the usual phonon gas model result for the diffusivity [Eq. (10)]. Applying concepts which date back to Einstein, they assumed the phonon mean free path to be equal to half the wavelength. Their result is in good agreement with the measured thermal conductivity. However the hypothesis

that $\ell \sim \lambda/2$ does not agree with the damping of the modes measured by IXS as shown in Sec. V A. In terms of the diffusivity, the assumption of $\ell \sim \lambda/2$ in the phonon gas model gives the curve plotted as a dotted line in Fig. 10. This diffusivity is clearly too high with respect to the one that can be extracted from the IXS dynamic structure factor, even when using Eq. (9).

Various assumptions at the base of the present thermal conductivity estimate need some further comments. A first strong assumption is the use of the Debye approximation for the density of states. This choice can be justified by the following argument: If the total density of states is used in Eq. (8), the thermal conductivity is overestimated in the region of the plateau. This is due to the presence of the excess of states at the boson peak, which is located at a frequency around 1 THz and corresponds to the temperature region between 10 and 40 K, thus in the upper part of the plateau. This modes are nondispersive, as shown in Sec. IV A, and for this reason they cannot be included in the evaluation based on Eq. (9), where only the diagonal elements of the heat current operator are used and a nonzero sound speed is required. For the same reason, the inclusion of the transverse modes in our estimate is also questionable, although unavoidable in the framework of the Debye approximation.

Probably the strongest assumption in the present evaluation is the omission of the off-diagonal contributions to the heat current operator. Unfortunately the off-diagonal elements necessary for a complete determination of the heat current operator are not experimentally accessible. Nevertheless the acousticlike excitations detected by the IXS technique in the terahertz frequency range give a substantial direct contribution to the thermal conductivity. The resulting heat conductivity is however "minimal"[34,36] because these high-frequency modes are strongly damped, with a mean free path of only a few angstroms. The mechanism of heat conduction is thus more similar to a diffusive process than to the ballistic regime described by the phonon gas model.[78]

VI. CONCLUSIONS

The combined use of IXS and INS has allowed the study of the dynamic structure factor of vitreous silica in a broad frequency-momentum region and in a wide temperature range, both below and above the glass transition. The results confirm the persistence of acousticlike excitations, characterized by the macroscopic longitudinal speed of sound, up to terahertz frequencies. When the wave vector is increased above 4 nm^{-1}, a second inelastic component appears in the IXS spectrum. The INS time-of-flight technique allows better resolution of the shape of the low-frequency peak, which is nondispersing and located around the boson peak frequency. In the same frequency region, the longitudinal mode shows a marked positive dispersion effect and its mean free path reaches values on the order of the interatomic spacing. The absence of temperature dependence suggests the structural disorder to be responsible for both the broadening of the longitudinal peak and its shift with respect to a linear dispersion. As the wave vector is increased, the coherence content in the dynamic structure factor tends to fade out. The spectra then merge in an effective density of vibrational states.

A detailed line-shape analysis of the IXS and INS spectra allows a sensible determination of the various parameters describing the observed spectral features. The integrated intensity of the modes in the low wave-vector region can be qualitatively described in terms of a simple plane-wave-like harmonic model.

We have then computed the contribution of the terahertz vibrations to the heat transport in the framework of the thermal Kubo equation. The acousticlike modes contribute a non-negligible diffusivity that can account for a relevant fraction of the measured high-temperature thermal conductivity. A diffusivelike heat transport process between different eigenvectors can be invoked to explain the missed thermal conductivity, as suggested by Allen and Feldman.[40]

ACKNOWLEDGMENTS

G.B. is indebted to U. Buchenau for many fruitful discussions on the thermal conductivity in amorphous solids. C. Henriquet is kindly acknowledged for his support in the preparation of the high-temperature setup for the IXS experiment. The authors thank A. J. Dianoux for his help during the neutron experiment at IN6. E.F. acknowledges M. M. Koza for his support in the treatment of the neutron data. Technical and financial support from the ILL facility is gratefully acknowledged.

*giacomo.baldi@esrf.fr

[1] R. C. Zeller and R. O. Pohl, Phys. Rev. B **4**, 2029 (1971).
[2] C. A. Angell, Science **267**, 1924 (1995).
[3] R. E. Strakna and H. T. Savage, J. Appl. Phys. **35**, 1445 (1964).
[4] A. S. Pine, Phys. Rev. **185**, 1187 (1969).
[5] W. Dietsche and H. Kinder, Phys. Rev. Lett. **43**, 1413 (1979).
[6] B. Golding, J. E. Graebner, and R. J. Schutz, Phys. Rev. B **14**, 1660 (1976).
[7] J. M. Carpenter and D. L. Price, Phys. Rev. Lett. **54**, 441 (1985); D. L. Price and J. M. Carpenter, J. Non-Cryst. Solids **92**, 153 (1987).
[8] U. Buchenau, N. Nücker, and A. J. Dianoux, Phys. Rev. Lett. **53**, 2316 (1984); U. Buchenau, M. Prager, N. Nücker, A. J. Dianoux, N. Ahmad, and W. A. Phillips, Phys. Rev. B **34**, 5665 (1986).
[9] T. C. Zhu, H. J. Maris, and J. Tauc, Phys. Rev. B **44**, 4281 (1991).
[10] M. Arai, A. C. Hannon, A. D. Taylor, T. Otomo, A. C. Wright, R. N. Sinclair, and D. L. Price, Trans. Am. Crystallogr. Assoc. **27**, 113 (1991); M. Arai, A. C. Hannon, A. D. Taylor, A. C. Wright, R. N. Sinclair, and D. L. Price, Physica B (Amsterdam) **180**, 779 (1992).
[11] M. Arai, Y. Inamura, T. Otomo, N. Kitamura, S. M. Bennington, and A. C. Hannon, Physica B (Amsterdam) **263-264**, 268

(1999); M. Nakamura, M. Arai, Y. Inamura, T. Otomo, and S. M. Bennington, Phys. Rev. B **67**, 064204 (2003).
[12] M. Foret, E. Courtens, R. Vacher, and J.-B. Suck, Phys. Rev. Lett. **77**, 3831 (1996).
[13] P. Benassi, M. Krisch, C. Masciovecchio, V. Mazzacurati, G. Monaco, G. Ruocco, F. Sette, and R. Verbeni, Phys. Rev. Lett. **77**, 3835 (1996).
[14] B. Ruzicka, T. Scopigno, S. Caponi, A. Fontana, O. Pilla, P. Giura, G. Monaco, E. Pontecorvo, G. Ruocco, and F. Sette, Phys. Rev. B **69**, 100201(R) (2004).
[15] P. Benassi, S. Caponi, R. Eramo, A. Fontana, A. Giugni, M. Nardone, M. Sampoli, and G. Viliani, Phys. Rev. B **71**, 172201 (2005).
[16] C. Masciovecchio, G. Baldi, S. Caponi, L. Comez, S. Di Fonzo, D. Fioretto, A. Fontana, A. Gessini, S. C. Santucci, F. Sette, G. Viliani, P. Vilmercati, and G. Ruocco, Phys. Rev. Lett. **97**, 035501 (2006).
[17] T. Nakayama, Rep. Prog. Phys. **65**, 1195 (2002), and references therein.
[18] W. Jin, P. Vashishta, R. K. Kalia, and J. P. Rino, Phys. Rev. B **48**, 9359 (1993).
[19] S. N. Taraskin and S. R. Elliott, Europhys. Lett. **39**, 37 (1997); S. N. Taraskin and S. R. Elliott, Phys. Rev. B **56**, 8605 (1997); S. N. Taraskin and S. R. Elliott, Philos. Mag. B **77**, 403 (1998).
[20] R. Dell'Anna, G. Ruocco, M. Sampoli, and G. Viliani, Phys. Rev. Lett. **80**, 1236 (1998); O. Pilla, S. Caponi, A. Fontana, J. R. Goncalves, M. Montagna, F. Rossi, G. Viliani, L. Angelani, G. Ruocco, G. Monaco, and F. Sette, J. Phys.: Condens. Matter **16**, 8519 (2004).
[21] A. Pasquarello, J. Sarnthein, and R. Car, Phys. Rev. B **57**, 14133 (1998); A. Pasquarello, *ibid.* **61**, 3951 (2000).
[22] J. Horbach, W. Kob, and K. Binder, Eur. Phys. J. B **19**, 531 (2001).
[23] L. Giacomazzi and A. Pasquarello, J. Phys.: Condens. Matter **19**, 415112 (2007).
[24] G. Ruocco and F. Sette, J. Phys.: Condens. Matter **13**, 9141 (2001).
[25] F. Sette, G. Ruocco, M. Krisch, C. Masciovecchio, R. Verbeni, and U. Bergmann, Phys. Rev. Lett. **77**, 83 (1996); G. Monaco, A. Cunsolo, G. Ruocco, and F. Sette, Phys. Rev. E **60**, 5505 (1999); E. Pontecorvo, M. Krisch, A. Cunsolo, G. Monaco, A. Mermet, R. Verbeni, F. Sette, and G. Ruocco, *ibid.* **71**, 011501 (2005).
[26] T. Scopigno, E. Pontecorvo, R. Di Leonardo, M. Krisch, G. Monaco, G. Ruocco, B. Ruzicka, and F. Sette, Philos. Mag. **84**, 1453 (2004).
[27] T. Scopigno, R. Di Leonardo, G. Ruocco, A. Q. R. Baron, S. Tsutsui, F. Bossard, and S. N. Yannopoulos, Phys. Rev. Lett. **92**, 025503 (2004).
[28] T. Ichitsubo, S. Hosokawa, K. Matsuda, E. Matsubara, N. Nishiyama, S. Tsutsui, and A. Q. R. Baron, Phys. Rev. B **76**, 140201(R) (2007).
[29] A. Polian, Dung Vo-Thanh, and P. Richet, Europhys. Lett. **57**, 375 (2002).
[30] W. Götze and M. R. Mayr, Phys. Rev. E **61**, 587 (2000).
[31] S.-H. Chong, Phys. Rev. E **74**, 031205 (2006).
[32] G. Ruocco, F. Sette, R. Di Leonardo, G. Monaco, M. Sampoli, T. Scopigno, and, G. Viliani, Phys. Rev. Lett. **84**, 5788 (2000).
[33] C. Kittel, Phys. Rev. **75**, 972 (1949).
[34] G. A. Slack, in *Solid State Physics*, edited by H. Ehrenreich, F. Seitz, and D. Turnbull (Academic, New York, 1979), Vol. 34, p. 1.
[35] D. G. Cahill and R. O. Pohl, Phys. Rev. B **35**, 4067 (1987).
[36] D. G. Cahill and R. O. Pohl, Annu. Rev. Phys. Chem. **39**, 93 (1988); D. G. Cahill and R. O. Pohl Solid State Commun. **70**, 927 (1989); D. G. Cahill, S. K. Watson, and R. O. Pohl, Phys. Rev. B **46**, 6131 (1992).
[37] M. S. Love and A. C. Anderson, Phys. Rev. B **42**, 1845 (1990).
[38] A. Jagannathan, R. Orbach, and O. Entin-Wohlman, Phys. Rev. B **39**, 13465 (1989); J. Michalski, *ibid.* **45**, 7054 (1992).
[39] P. Sheng and M. Zhou, Science **253**, 539 (1991).
[40] P. B. Allen and J. L. Feldman, Phys. Rev. B **48**, 12581 (1993).
[41] C. Masciovecchio, U. Bergmann, M. Krisch, G. Ruocco, F. Sette, and R. Verbeni, Nucl. Instrum. Methods Phys. Res. B **111**, 181 (1996); C. Masciovecchio, U. Bergmann, M. Krisch, G. Ruocco, F. Sette, and R. Verbeni, *ibid.* **117**, 339 (1996); R. Verbeni, F. Sette, M. Krisch, U. Bergmann, B. Gorges, C. Halcoussis, K. Martel, C. Masciovecchio, J. F. Ribois, G. Ruocco, and H. Sinn, J. Synchrotron Radiat. **3**, 62 (1996).
[42] G. Hetherington and K. H. Jack, *Ullmans Encyklopedie der Technischen Chemie*, 3rd ed. (Urban & Schwarzenberg, München, Berlin, 1963), Vol. 14, pp. 511–524.
[43] R. Böhmer, K. L. Ngai, C. A. Angell, and D. J. Plazek, J. Chem. Phys. **99**, 4201 (1993).
[44] A. Wischnewski, U. Buchenau, A. J. Dianoux, W. A. Kamitakahara, and J. L. Zarestky, Phys. Rev. B **57**, 2663 (1998); A. Fontana, R. Dell'Anna, M. Montagna, F. Rossi, G. Viliani, G. Ruocco, M. Sampoli, U. Buchenau, and A. Wischnewski, Europhys. Lett. **47**, 56 (1999).
[45] H. Ehrenreich and L. Schwarts, in *Solid State Physics*, edited by H. Ehrenreich, F. Seitz, and D. Turnbull (Academic, New York, 1976), Vol. 31, p. 149.
[46] E. N. Economou, *Green's Functions in Quantum Physics*, 2nd ed. (Springer-Verlag, New York, 1983).
[47] V. Martin-Mayor, G. Parisi, and P. Verrocchio, Phys. Rev. E **62**, 2373 (2000); T. S. Grigera, V. Martin-Mayor, G. Parisi, and P. Verrocchio, Phys. Rev. Lett. **87**, 085502 (2001); V. Martin-Mayor, M. Mezard, G. Parisi, and P. Verrocchio, J. Chem. Phys. **114**, 8068 (2001); S. Ciliberti, T. S. Grigera, V. Martin-Mayor, G. Parisi, and P. Verrocchio, *ibid.* **119**, 8577 (2003).
[48] S. N. Taraskin and S. R. Elliott, J. Phys.: Condens. Matter **14**, 3143 (2002).
[49] W. Schirmacher, G. Ruocco, and T. Scopigno, Phys. Rev. Lett. **98**, 025501 (2007); W. Schirmacher, B. Schmid, C. Tomaras, G. Viliani, G. Baldi, G. Ruocco, and T. Scopigno, Phys. Status Solidi C **5**, 862 (2008).
[50] R. L. Mozzi and B. E. Warren, J. Appl. Crystallogr. **2**, 164 (1969); A. Pierre, D. R. Uhlmann, and F. N. Molea, *ibid.* **5**, 216 (1972); T. Watanabe, K. Saito, and, A. J. Ikushima, J. Appl. Phys. **94**, 4824 (2003); C. Levelut, A. Faivre, R. Le Parc, B. Champagnon, J.-L. Hazemann, and J.-P. Simon, Phys. Rev. B **72**, 224201 (2005); C. Levelut, R. Le Parc, A. Faivre, R. Brüning, B. Champagnon, V. Martinez, J.-P. Simon, F. Bley, and J.-L. Hazemann, J. Appl. Crystallogr. **40**, s512 (2007).
[51] P. A. V. Johnson, A. C. Wright, and R. N. Sinclair, J. Non-Cryst. Solids **58**, 109 (1983); S. Susman, K. J. Volin, D. G. Montague, and D. L. Price, Phys. Rev. B **43**, 11076 (1991).
[52] V. K. Malinovsky, V. N. Nokikov, P. P. Parshin, A. P. Sokolov, and M. G. Zemlyanov, Europhys. Lett. **11**, 43 (1990); V. K. Malinovsky, V. N. Nokikov, and A. P. Sokolov, Phys. Lett. A

153, 63 (1991).
[53] T. Scopigno, Laurea Thesis, L'Aquila University, 1998; C. Masciovecchio, V. Mazzacurati, G. Monaco, G. Ruocco, T. Scopigno, F. Sette, P. Benassi, A. Cunsolo, A. Fontana, M. Krisch, A. Mermet, M. Montagna, F. Rossi, M. Sampoli, G. Signorelli, and R. Verbeni, Philos. Mag. B **79**, 2013 (1999).
[54] O. Pilla, A. Cunsolo, A. Fontana, C. Masciovecchio, G. Monaco, M. Montagna, G. Ruocco, T. Scopigno, and F. Sette, Phys. Rev. Lett. **85**, 2136 (2000); O. Pilla, S. Caponi, A. Fontana, M. Montagna, L. Righetti, F. Rossi, G. Viliani, G. Ruocco, G. Monaco, F. Sette, R. Verbeni, G. Cicognani, and A. J. Dianoux, Philos. Mag. B **82**, 223 (2002).
[55] G. Winterling, Phys. Rev. B **12**, 2432 (1975); A. P. Sokolov, V. N. Novikov, and B. Strube, Europhys. Lett. **38**, 49 (1997); J. Wiedersich, N. V. Surovtsev, V. N. Novikov, E. Rössler, and A. P. Sokolov, Phys. Rev. B **64**, 064207 (2001); S. Caponi, A. Fontana, F. Rossi, G. Baldi, and E. Fabiani, *ibid.* **76**, 092201 (2007).
[56] U. Buchenau, H. M. Zhou, N. Nucker, K. S. Gilroy, and W. A. Phillips, Phys. Rev. Lett. **60**, 1318 (1988); A. Fontana, F. Rossi, S. Caponi, E. Fabiani, U. Buchenau, and A. Wischnewski, J. Non-Cryst. Solids **351**, 1928 (2005).
[57] This function is more correctly the convolution of the inelastic part of the longitudinal current with the resolution function $\frac{\omega^2}{q^2} I_{\mathrm{inel}}(q,\omega) = C_{\mathrm{inel}}(q,\omega) \otimes R(\omega)$.
[58] M. Sampoli, G. Ruocco, and F. Sette, Phys. Rev. Lett. **79**, 1678 (1997).
[59] M. T. Dove, M. J. Harris, A. C. Hannon, J. M. Parker, I. P. Swainson, and M. Gambhir, Phys. Rev. Lett. **78**, 1070 (1997).
[60] M. Nakamura, M. Arai, T. Otomo, Y. Inamura, and S. M. Bennington, J. Non-Cryst. Solids **293-295**, 377 (2001); M. Nakamura, M. Arai, Y. Inamura, T. Otomo, and S. M. Bennington, Phys. Rev. B **66**, 024203 (2002).
[61] B. Hehlen, E. Courtens, R. Vacher, A. Yamanaka, M. Kataoka, and K. Inoue, Phys. Rev. Lett. **84**, 5355 (2000).
[62] J. J. Freeman and A. C. Anderson, Phys. Rev. B **34**, 5684 (1986); C. C. Yu and J. J. Freeman, *ibid.* **36**, 7620 (1987).
[63] J. E. Graebner, B. Golding, and L. C. Allen, Phys. Rev. B **34**, 5696 (1986).
[64] A. C. Anderson, in *Amorphous Solids, Low Temperature Properties*, edited by W. A. Phillips (Springer, New York, 1981).
[65] U. Buchenau, Yu. M. Galperin, V. L. Gurevich, D. A. Parshin, M. A. Ramos, and H. R. Schober, Phys. Rev. B **46**, 2798 (1992).
[66] R. Vacher, J. Pelous, and E. Courtens, Phys. Rev. B **56**, R481 (1997).
[67] W. Schirmacher, Europhys. Lett. **73**, 892 (2006).
[68] R. O. Pohl, X. Liu, and E. Thompson, Rev. Mod. Phys. **74**, 991 (2002).
[69] A. F. Ioffe and A. R. Regel, Prog. Semicond. **4**, 237 (1960).
[70] The parameter $\Gamma(q)$ of the DHO model in Eq. (4) is the FWHM of the peak for $q \to 0$.
[71] G. Ruocco, F. Sette, R. Di Leonardo, D. Fioretto, M. Krisch, M. Lorenzen, C. Masciovecchio, G. Monaco, F. Pignon, and T. Scopigno, Phys. Rev. Lett. **83**, 5583 (1999).
[72] J. K. Flicker and P. L. Leath, Phys. Rev. B **7**, 2296 (1973).
[73] A. Alam and A. Mookerjee, Phys. Rev. B **72**, 214207 (2005).
[74] The Boltzmann equation for the thermal conductivity is reviewed in many textbooks. See, e.g., J. Callaway, *Quantum Theory of the Solid State*, 2nd ed. (Academic, New York, 1991).
[75] R. Vacher, J. Pelous, F. Plique, and A. Zarembowitch, J. Non-Cryst. Solids **45**, 397 (1981).
[76] S. N. Taraskin and S. R. Elliott, Phys. Rev. B **61**, 12031 (2000).
[77] A simplified expression is often used in the literature (Ref. 37). In these evaluations the diffusivity is assumed to be given by the product of an average sound velocity, usually the Debye one, and of the longitudinal mean free path. In the Debye approximation for vitreous silica, this is approximately equivalent to assuming the same value for the longitudinal and the transverse mean free paths. This simplified approach thus gives a slightly higher conductivity compared to our estimate.
[78] J. L. Feldman, M. D. Kluge, P. B. Allen, and F. Wooten, Phys. Rev. B **48**, 12589 (1993).